

# X-rays and hard ultraviolet radiation from the first galaxies: ionization bubbles and 21-cm observations

Aparna Venkatesan<sup>1</sup>\* and Andrew Benson<sup>2</sup>

<sup>1</sup>*Department of Physics and Astronomy, University of San Francisco, 2130 Fulton Street, San Francisco, CA 94117, USA*

<sup>2</sup>*California Institute of Technology, MC 350-17, 1200 East California Boulevard, Pasadena, CA 91125, USA*

Accepted 2011 July 7. Received 2011 July 5; in original form 2011 February 26

## ABSTRACT

The first stars and quasars are known sources of hard ionizing radiation in the first billion years of the Universe. We examine the joint effects of X-rays and hard ultraviolet (UV) radiation from such first-light sources on the hydrogen and helium reionization of the intergalactic medium (IGM) at early times, and the associated heating. We study the growth and evolution of individual H II, He II and He III regions around early galaxies with first stars and/or quasi-stellar object populations. We find that in the presence of helium-ionizing radiation, X-rays may not dominate the ionization and thermal history of the IGM at  $z \sim 10$ –20, contributing relatively modest increases to IGM ionization and heating up to  $\sim 10^3$ – $10^5$  K in IGM temperatures. We also calculate the 21-cm signal expected from a number of scenarios with metal-free starbursts and quasars in varying combinations and masses at these redshifts. The peak values for the spin temperature reach  $\sim 10^4$ – $10^5$  K in such cases. The maximum values for the 21-cm brightness temperature are around 30–40 mK in emission, while the net values of the 21-cm absorption signal range from  $\sim$ a few to 60 mK on scales of 0.01–1 Mpc. We find that the 21-cm signature of X-ray versus UV ionization could be distinct, with the emission signal expected from X-rays alone occurring at smaller scales than that from UV radiation, resulting from the inherently different spatial scales at which X-ray and UV ionization/heating manifests. This difference is time-dependent and becomes harder to distinguish with an increasing X-ray contribution to the total ionizing photon production. Such differing scale-dependent contributions from X-ray and UV photons may therefore ‘blur’ the 21-cm signature of the percolation of ionized bubbles around early haloes (depending on whether a cosmic X-ray or UV background is built up first) and affect the interpretation of 21-cm data constraints on reionization.

**Key words:** stars: Population III – galaxies: high-redshift – intergalactic medium – quasars: general – cosmology: theory – dark ages, reionization, first stars.

## 1 INTRODUCTION

The first billion years after the big bang represent a period of great interest for studies of both galaxy formation and the evolution of the Universe as a whole. This period sees the formation of the first galaxies (Wise, Turk & Abel 2008) and, consequently, the beginning and completion of the process of reionizing the Universe (Loeb & Barkana 2001; Loeb 2009) as a result of the copious number of ionizing photons emitted by these sources. Current and future facilities aim to probe this epoch of the Universe both using traditional methods, such as surveying faint galaxies (e.g. *The James Webb Space Telescope*; Gardner et al. 2009), and using novel techniques such as 21-cm cosmology (Furlanetto, Oh & Briggs 2006) to probe

the distribution of neutral hydrogen during the process of reionization. Understanding this epoch of the Universe from a theoretical perspective therefore requires an understanding both of the sources of ionizing photons and of the thermal and ionization states of the intergalactic medium (IGM) at these times.

Additionally, the thermal and ionization history of the IGM as a function of cosmic redshift,  $z$ , strongly affects the ‘visibility’ of the most distant galaxies and quasars (Madau 1995; Meiksin 2006; Dayal, Maselli & Ferrara 2011), and the feedback exerted on the formation of new galaxies (Efstathiou 1992; Quinn, Katz & Efstathiou 1996; Navarro & Steinmetz 1997; Barkana & Loeb 1999; Bullock, Kravtsov & Weinberg 2000; Benson et al. 2002a,b; Somerville 2002; Koposov et al. 2009; Muoz et al. 2009; Busha et al. 2010; Macci et al. 2010). The process of reionization is expected to begin with the formation of ionized bubbles around luminous sources in the redshift range  $z = 10$ –20. These bubbles will eventually grow

\*E-mail: avenkatesan@usfca.edu

in size and number until complete overlap is reached and the Universe becomes fully reionized. The shapes and sizes of bubbles will be controlled by the cosmological density field and the process of galaxy formation. Their internal ionization and temperature structure will depend on the spectrum of the input source (i.e. how hard the photons are) and the efficiencies of recombination and cooling processes.

The recent data from the *WMAP-7* (Larson et al. 2011) reveal that the IGM is fully ionized up to  $z \sim 10$ , most likely with a period of partial ionization at higher redshifts. Theoretical work over the last 15 years has focused mostly on the hydrogen reionization of the IGM (Gnedin & Ostriker 1997; Chiu & Ostriker 2000; Ciardi et al. 2000; Somerville, Bullock & Livio 2003; Onken & Miralda-Escudé 2004; Benson et al. 2006; Furlanetto et al. 2006). However, helium reionization has received comparatively less attention, ranging from calculations of helium/hydrogen reionization from the first stars and quasi-stellar objects (QSOs) at  $z \gtrsim 6$  (Venkatesan, Tumlinson & Shull 2003; Wyithe & Loeb 2003) to studies of helium reionization by QSOs at  $z \sim 3$  (Sokasian et al. 2003; Furlanetto & Oh 2008a,b). Although helium is the second most abundant element, its substantially higher ionization energy relative to hydrogen, as well as its interactions with X-rays through secondary ionizations, can lead to significant effects for the high- $z$  IGM and the cosmic microwave background (CMB) once reionization has occurred even to a partial degree. Additionally, X-rays have greater penetrating power relative to ultraviolet (UV) radiation. When occurring in combination with helium ionization from the first stars and quasars, X-rays could act to strongly alter the ionization and thermal history of the IGM.

In this work, we investigate the joint impact of X-rays and helium-ionizing radiation from the first galaxies on IGM reionization and heating. We focus on the growth and evolution of individual ionization fronts (I-fronts) in H and He, rather than a fully evolving cosmological calculation, which we plan to pursue in future work (Section 4). We study whether the differing contributions arising from X-ray versus UV ionization can be distinguished through 21-cm observations. Recent papers by other authors have focused on specific aspects of this problem in other contexts, for example, helium reionization by quasars at lower redshifts ( $z \sim 3$ ) (Furlanetto & Oh 2008b; Bolton, Oh & Furlanetto 2009; McQuinn et al. 2009), without explicitly considering the effects of X-ray heating (Furlanetto & Oh 2008a) or with only a single high-mass star embedded in a high- $z$  galaxy halo (Chen & Miralda-Escudé 2008). We will demonstrate that X-rays *may not* play a dominant role in high- $z$  ionization, contrary to the theoretical expectations in some previous works (see e.g. Thomas & Zaroubi 2008), and will ask the question: does there exist a cosmological epoch when the IGM's thermodynamic and ionization properties are determined mostly by X-rays?

The trade-off of these ionization effects will have important consequences for predictions for future radio observations that plan to see ionized bubbles in emission or absorption against the CMB. There has already been a substantial body of work on the feedback on ionization (Tumlinson et al. 2003; Venkatesan, Tumlinson & Shull 2003; Wyithe & Loeb 2003) and emission-line signatures (Oh, Haiman & Rees 2001; Tumlinson, Giroux & Shull 2001; Venkatesan, Tumlinson & Shull 2003; Dawson et al. 2007) arising from first-light sources that have hard ionizing spectra. Here, we focus on the radio signatures as the topology of reionization arising from X-rays versus UV radiation is expected to be different. We also test other theoretical predictions for the growth of individual ionized regions around early galaxies, for example, the H and

He I fronts may track each other closely for sufficiently hard sources such as the first stars and QSOs.

The remainder of this paper is arranged as follows. In Section 2, we describe the model that we use to follow the growth of cosmological I-fronts around evolving sources. In Section 3, we present our results for the thermal and ionization properties of such regions, their observable signatures (including 21-cm signals) around a set of representative sources, and compare our findings with earlier works in this field. We then conclude in Section 4.

## 2 BACKGROUND AND MODELS

We assume a background cosmology using the most recent cosmological parameter fits from the *WMAP-7* CMB data (Larson et al. 2011). We combine the formalisms for studying the non-equilibrium evolution of hydrogen and helium in the IGM in Venkatesan et al. (2003) and Tumlinson, Venkatesan & Shull (2004), and the input processes related to X-ray ionization in the high- $z$  IGM in Venkatesan, Giroux & Shull (2001) with the code `GALACTICUS`. `GALACTICUS` is a newly developed semi-analytic code on galaxy formation (Benson 2011) which includes feedback from high-redshift star/quasar formation while meeting current experimental constraints at lower redshifts. Here, we have utilized it to solve for the growth of a spherical I-front around a point source in the IGM. The ionizing and heating processes included in this code are described in detail below.

We are primarily interested in the effects of hard ionizing radiation from the first galaxies – these are assumed to be of the order of  $10^8 M_\odot$  in total mass and of approximate size 1 to a few kpc.<sup>1</sup> We follow the advancing ionized fractions<sup>2</sup> around a starburst and/or quasar in such a halo and treat the IGM as being homogenous around the source. In particular, we do not include a density enhancement as would be expected if the source forms in the centre of a dark matter halo. In general, the I-fronts we find are much larger in size than typical haloes at these redshifts and so will be insensitive to the details of the density profile on small scales. Additionally, sources such as those considered here will likely form in haloes sufficiently massive to collisionally ionize hydrogen and helium, such that the photoI-front would begin growing from the edge of the collisionally ionized region.<sup>3</sup>

We consider quasars with varying black hole (BH) masses and model a typical QSO spectrum with the fit given in Haardt & Madau (1996). We assume that the duty cycle of the QSO is 100 million years typically – significantly longer duty cycles would exceed the Hubble time at  $z \sim 10$ –20. In our models, we allow the active galactic nucleus (AGN) to be on for 100 Myr before it is shut off.

<sup>1</sup> A  $10^{10} M_\odot$  halo at  $z = 10$  has an approximate physical (not comoving) virial radius of  $\sim 7$  kpc, with a galaxy of size  $\sim 1$  kpc in it. A massive Milky Way mass halo ( $10^{12} M_\odot$ ) at that redshift would be of size about 33 kpc, with a typical galaxy of a few kpc in size.

<sup>2</sup> This is in contrast to Venkatesan et al. (2001), where the average IGM ionization fraction was computed without tracking the growth of individual I-fronts around the haloes containing the QSO.

<sup>3</sup> In a fully 3D calculation, these haloes would accrete most of their mass via cold filaments of gas which are not shock heated as they enter the halo and so are not collisionally ionized. It is beyond the scope of this work to examine the effect of such filaments on the growth of I-fronts (Kereš et al. 2005), but they can be expected to impede the growth of the front along directions coinciding with a filament, while permitting faster growth along directions between filaments.

We include the effects of metal-free stars occurring in starbursts of varying masses – the fits are taken from Venkatesan et al. (2003).

The non-equilibrium ionization fractions are calculated including the following processes: photoionization, collisional ionization, case B radiative recombination, dielectronic recombination for He I, and the coupling between H and He caused by the radiation fields from the He I 24.6-eV recombination continuum and from the bound–bound transitions of He I (Venkatesan et al. 2001). The photoionization cross-sections for H I and He II are taken from Spitzer (1978), and from Verner et al. (1996) for He I. The ratio of the H I to He I photoionization cross-sections decreases with photon energy, ranging from about 5 per cent at 100 eV to 3.5 per cent at 1 keV. This implies that an X-ray photon is ‘seen’ better by a He I atom than by a H I atom.

We also include secondary ionizations and excitations of H I and He I arising from the X-rays (Shull & van Steenberg 1985). As noted in Venkatesan et al. (2001), a typical X-ray photon is far more likely to be absorbed by He I rather than H I, so that secondary ionization (rather than direct photoionization) is most relevant for H I when X-rays dominate photoionization. The resulting photoelectrons will ionize many more H I atoms than He I, H I atoms being more numerous. As the background ionization increases, the photoelectron deposits more and more of its energy in heat and less in collisional ionizations/excitations. Shull & van Steenberg (1985) assumed that the ionization fractions of H I and He I were equal, and we have replaced the generic ionization fraction in their formulae with the electron fraction  $x_e$  which is more directly relevant for the IGM.

The thermal evolution of the gas is computed including the following processes (Venkatesan et al. 2001): photoelectric heating from the secondary electrons of H and He, which is itself a function of the background ionization levels (Shull & van Steenberg 1985) and heating from the H I photoelectrons liberated by the bound–bound transitions or the 24.6-eV recombination continuum of He I. Cooling terms include radiative and dielectronic recombination (Venkatesan et al. 2001, and references therein), thermal bremsstrahlung, Compton scattering off the CMB, collisional ionization and excitation, and the adiabatic expansion of the IGM. The contribution to heating and cooling from the scattering of the secondary Ly $\alpha$  photons from X-ray ionization is negligible (Chen & Miralda-Escudé 2004, 2008) and is not included here.

Our 1D non-equilibrium ionization code includes all of the above ionization and heating processes, and solves for the evolution of the thermal and ionization states around the source as follows. The IGM surrounding the source is divided up into a large number of concentric spherical shells. Unless otherwise noted, we use 1000 shells, spaced logarithmically in radius from  $10^{-4}$  to 10 Mpc. These shells are initially populated with hydrogen and helium in a primordial ratio.

When considering a uniform medium surrounding the source, the gas is given initial ionized fractions as determined by the RECFast recombination code<sup>4</sup> (Seager, Sasselov & Scott 2000) for the appropriate cosmology and redshift. The initial temperature of the gas in each shell is also determined by RECFast and each shell is initially set to be expanding with the Hubble flow.

We then proceed to evolve the thermal and ionization states of these shells forwards in time in a series of short time-steps. During each time-step, we begin by computing the input spectrum of photons emitted by the central source (QSO, stars or both). Given

this spectrum, we compute rates of ionization and heating in the innermost shell and solve for the evolution of its properties by integrating the appropriate set of differential equations as described below. The input spectrum is then attenuated by the optical depth of this first shell and used as input for the second shell. This process is repeated until the outermost shell is reached (which is chosen to be at sufficiently large radius that the radiation field is attenuated to close to zero at all times during our calculation). In addition to changes in temperature and ionization states, the density of each shell evolves as it expands or contracts due to any initial velocity and pressure forces. This approach is similar to those in other recent papers, for example, Thomas & Zaroubi (2008).

Our calculations of the ionization and thermal evolution of each shell use the same input physics as the IGM evolution model of Benson & Bower (2010). The density of each ionization,  $n_i$ , state in a given shell is then given by

$$\begin{aligned} \frac{dn_i}{dt} = & -n_i \frac{\dot{V}}{V} + [\alpha_i(T)n_{i+1}n_e - \alpha_{i-1}(T)n_i n_e \\ & - \Gamma_{e,i}(T)n_i n_e + \Gamma_{e,i-1}(T)n_{i-1}n_e - \Gamma_{\gamma,i}n_i \\ & + \Gamma_{\gamma,i-1}n_{i-1}], \end{aligned} \quad (1)$$

where for each atomic species H or He,  $i$  refers to their ionization state (i.e.  $i = 1$  and  $2$  for H and  $H^+$ , and  $i = 3, 4$  and  $5$  for He,  $He^+$  and  $He^{2+}$ , respectively),  $n_i$  is the number density,  $T$  is the temperature of the shell,  $V$  is the volume of the shell,  $\alpha_i$  is the recombination rate for  $i$  (Verner & Ferland 1996),  $\Gamma_{e,i}$  is the collisional ionization rate coefficient for  $i$  (Voronov 1997) and  $\Gamma_{\gamma,i}$  is the photoionization rate for  $i$  which is given by

$$\Gamma_{\gamma,i} = \int_0^\infty \sigma'_i(E)n_i \frac{S_\gamma(E)e^{-\tau(E;r)}}{4\pi r^2} dE, \quad (2)$$

where  $\sigma'_i$  is an effective photoionization cross-section that accounts for the effects of secondary ionizations and is given by Shull & van Steenberg (1985) (as re-expressed by Venkatesan et al. 2001):

$$\begin{aligned} \sigma'_H(E) = & \left(1 + \phi_{H1} \frac{E - E_H}{E_H} + \phi_{He1}^* \frac{E - E_H}{19.95 \text{ eV}}\right) \sigma_H(E) \\ & + \left(1 + \phi_{He1} \frac{E - E_{He}}{E_{He}}\right) \sigma_{He}(E), \end{aligned} \quad (3)$$

$$\begin{aligned} \sigma'_{He}(E) = & \left(1 + \phi_{He1} \frac{E - E_{He}}{E_{He}}\right) \sigma_{He}(E) \\ & + \left(\phi_{He1} \frac{E - E_H}{24.6 \text{ eV}}\right) \sigma_H(E), \end{aligned} \quad (4)$$

where  $\sigma(E)$  is the actual cross-section (Verner & Yakovlev 1995), and

$$\phi_{H1} = 0.3908 \left(1 - x_e^{0.4092}\right)^{1.7592}, \quad (5)$$

$$\phi_{He1}^* = 0.0246 \left(1 - x_e^{0.4049}\right)^{1.6594}, \quad (6)$$

$$\phi_{He1} = 0.0554 \left(1 - x_e^{0.4614}\right)^{1.6660}. \quad (7)$$

In the above,  $S(E) dE$  is the number of photons emitted per second in the energy range  $E$  to  $E + dE$  by the central source and  $\tau(E; r)$  is the optical depth to radius  $r$  at energy  $E$ .

Similarly, the evolution of the temperature of each shell is given by

$$\frac{dT}{dt} = -(\gamma - 1)T \frac{\dot{V}}{V} + \frac{T}{\mu} \frac{d\mu}{dt} + \frac{(\Sigma^T - \Lambda^T)}{\frac{3}{2}k_B n_{\text{tot}}}. \quad (8)$$

<sup>4</sup> We use v1.4.2 of RECFast and include all of the modifications to the He I recombination rate.

Here,  $\gamma$  is the adiabatic index of the gas,  $\Sigma^T$  is the rate of heating per unit volume due to all the heat sources (i.e. Compton heating and photoheating) and  $\Lambda^T$  is the rate of cooling per unit volume due to all the heat sinks (i.e. bremsstrahlung cooling and various atomic processes),  $n_{\text{tot}}$  is the total number density of atoms (H and He) and their ions per unit volume,  $T$  is the temperature of the shell and  $k_B$  is Boltzmann constant.

In the above equation, the first term represents adiabatic cooling due to the expansion of the shell. The second term accounts for the effects of changes in the mean atomic mass due to ionization and recombination processes. The final term accounts for the heating and cooling effects of the various processes that we now discuss below.

### Photoheating

Photoionization heats the shell at a rate of

$$\Sigma_{\text{photo}} = \int_0^\infty (E - E_i) \sigma'(E) n_i \frac{S_\gamma(E) e^{-\tau(E,r)}}{4\pi r^2} \mathcal{E} dE, \quad (9)$$

where  $E_i$  is the energy of the sampled photons which is associated with atom/ion number density  $n_i$ ,  $\sigma'$  is the effective partial photoionization cross-section (accounting for secondary ionizations) for the ionization stages of H and He,  $n_{\gamma(E)}$  is the number density of photons of energy  $E$ , and  $E_i$  is the ionization potential of  $i$ . In the above,  $\mathcal{E}$  accounts for heating by secondary electrons and is given by (Shull & van Steenberg 1985)

$$\mathcal{E} = 0.9971 \left[ 1 - \left( 1 - x_e^{0.2663} \right)^{1.3163} \right]. \quad (10)$$

### Compton cooling/heating

Compton scattering of CMB photons from free electrons causes cooling or heating of the gas at a rate of (Peebles 1968)

$$\Sigma_{\text{Compton}} = 4\sigma_T a_R [T_{\text{CMB}}(1+z)]^4 \frac{n_e k_B}{m_e c} [T_{\text{CMB}}(1+z) - T], \quad (11)$$

where  $\sigma_T$  is the Thomson cross-section,  $a_R$  is the radiation constant,  $T_{\text{CMB}}$  is the temperature of the CMB at  $z = 0$ ,  $n_e$  is the number density of electrons per unit volume and  $m_e$  is the mass of an electron.

For a typical source in our paper, we find that Compton heating is insignificant. The initial emission rate of ionizing photons for a  $10^5$ - $M_\odot$  starburst with a  $10^6$ - $M_\odot$  BH (detailed in the next section) is  $\sim 1.3 \times 10^{51}$  photons  $s^{-1}$ . The radius to which Compton heating is important (Ricotti, Ostriker & Mack 2008) for this scenario at  $z = 10$  is about 99 pc. As we will see, this is well below the 0.001–1 Mpc scales that are most relevant for I-front evolution and 21-cm signals in this work (Section 3); thus, Compton heating will not have a significant effect on our results.

### Single electron recombination cooling

Photon emission due to single electron recombination cools the shell at a rate

$$\Lambda_{\text{rec}} = \frac{3}{4} k_B T \left[ \alpha_{\text{H}^+}(T) n_{\text{H}^+} + \alpha_{\text{He}^+}(T) n_{\text{He}^+} + \alpha_{\text{He}^{2+}}(T) n_{\text{He}^{2+}} \right] n_e, \quad (12)$$

where  $\alpha_\tau$  is the rate of the recombination processes for its respective atom/ion number densities,  $n_i$  (Verner & Ferland 1996).

### Dielectric recombination cooling

Photon emission due to dielectric recombination cools the shell at a rate

$$\Lambda_{\text{dielec}} = 40.74 \text{ eV} \alpha_d(T) n_{\text{He}^{2+}} n_e, \quad (13)$$

where  $\alpha_d$  is the rate of the recombination process for  $\text{He}^{2+}$  (Aldrovandi & Pequignot 1973; Shull & van Steenberg 1982; Arnaud & Rothenflug 1985).

### Collisional ionization cooling

Collisional ionization leads to a cooling rate of

$$\Lambda_{\text{ion}} = \left[ E_{\text{H}} \alpha_{i_{\text{H}}}(T) n_{\text{H}} + E_{\text{He}} \alpha_{i_{\text{He}}}(T) n_{\text{He}} + E_{\text{He}^+} \alpha_{i_{\text{He}^+}}(T) n_{\text{He}^+} \right] n_e, \quad (14)$$

where  $\alpha_i$  is the collisional ionization rate coefficient for the respective atom/ion of number density  $n_i$  and  $E_i$  is the ionization potential of the respective atom/ion, H, He and  $\text{He}^+$ .

### Collisional excitation cooling

Collisional excitation followed by radiative decay cools the shell at a rate

$$\Lambda_{\text{ex}} = (\alpha_{\text{collH}} n_{\text{H}} + \alpha_{\text{collHe}^+} n_{\text{He}^+}) n_e, \quad (15)$$

where  $\alpha_{\text{collH}}$  and  $\alpha_{\text{collHe}^+}$  are the rates of collisional excitations involving H and  $\text{He}^+$ , respectively (Scholz & Walters 1991).

### Bremsstrahlung cooling

Finally, bremsstrahlung emission cools the shell at a rate

$$\Lambda_{\text{brem}} = \frac{16}{3\sqrt{3}} \left( \frac{2\pi k_B}{\hbar^2 m_e^3} \right)^{1/2} \left( \frac{e^2}{4c\pi\epsilon_0} \right)^3 c^2 \sqrt{T} [\gamma_{\text{H}^+}(T) n_{\text{H}^+} + \gamma_{\text{He}^+}(T) n_{\text{He}^+} + 4\gamma_{\text{He}^{2+}}(T) n_{\text{He}^{2+}}] n_e. \quad (16)$$

Here,  $\epsilon_0$  is the permittivity of free space and  $\gamma$  is the energy-averaged Gaunt factor (Sutherland 1998).

These coupled differential equations are solved numerically using a standard Runge–Kutta method.

## 3 RESULTS

As noted earlier, we focus on early galaxies of typical mass  $\sim 10^8$ – $10^{10} M_\odot$  (in total) and of approximate size a few kpc at most. We therefore perform most of our calculations at  $z = 10$ , with one calculation at  $z = 20$  for comparison.

To calculate the feedback from a typical QSO/star-forming galaxy at these epochs, we compute the BH mass function at  $z = 10$  using data that are publicly available from the Millennium Simulation data base<sup>5</sup> (Springel et al. 2005). In Fig. 1, we show the computed BH mass function at  $z = 10$ , where we see that a typical quasar is powered by BHs in the mass range  $\sim 10^5$ – $10^6 M_\odot$ , which we use as a baseline for most of the cases considered in this paper. The turnover in Fig. 1 may be partially due to the finite resolution of the simulation itself; in reality, we expect that the mass function should continue to slowly rise to somewhat smaller masses. In our models, the X-rays from the stellar populations are minimal, so we consider cases where the BH mass is typically  $10^6 M_\odot$ , with some lower BH mass cases (down to no BH) and one case with a BH mass of  $10^8 M_\odot$  to derive an upper limit to the X-ray feedback. We assume that the duty cycle of the QSO is 100 Myr for nearly all our cases but include one case with a low-mass BH QSO that has a shorter duty cycle of 10 Myr.

Note that the typical ratios of BH to stellar burst masses considered here are not consistent with the measured ratio of the BH to stellar spheroid (bulge) mass of 0.15 per cent at  $z = 0$  (Gültekin

<sup>5</sup> The Virgo-Millennium data base is available at: <http://www.gvo.org/Millennium/>

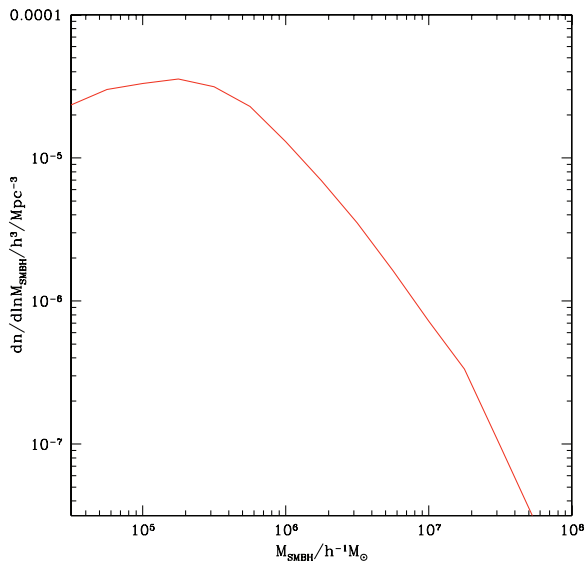


**Figure 1.** The BH mass function at  $z = 10$ , using public data from the Millennium Simulation data base. Note the peak around  $10^5$ – $10^6 M_\odot$ . See text for more discussion.

et al. 2009). Early galaxies differ from present-day ones in that they must have a seed BH that grows with time over generations of starbursts and galaxy mergers. Today we measure the BH-to-star (or spheroid) mass ratio *after* these processes have happened but it is unclear what this ratio would be for primordial galaxies, or if this ratio remains constant down to lower galaxy masses (Greene et al. 2010). AGN observations indicate a possible lag in the peak of BH growth (and therefore AGN activity) relative to the peak in the star formation rate in early galaxies, owing to gas dynamical effects between star formation and BH ‘feeding’ (Hopkins 2011). There are additional uncertainties related to the gas fraction, the Eddington ratio, etc., at high redshifts. Thus, we provide a few example cases here but do not attempt to provide a cosmological sample of model galaxies.

In order to distinguish the contributions of X-ray ionization relative to that from UV radiation, we consider three variations on each case with a starburst and QSO: one with the full spectrum including UV and X-ray photons from the source, one without the X-rays and one with the X-rays alone. To do this, we need to define the boundary between what is considered an X-ray versus a hard UV photon, a quantity that has often not been clearly defined in the cosmology literature on this topic (Ricotti, Ostriker & Gnedin 2005; Chen & Miralda-Escudé 2008). At least some of this difference arises from considering the spectrum at the source versus the emergent spectrum after processing through the gas in the galaxy. We choose 120 eV as the minimum threshold for what we consider an X-ray. This is consistent with the broader physics definition, but also with the impact of a typical X-ray on the IGM. We discuss this in detail in Section 3.3, but we note for now the well-known result that the mean free path (MFP) of X-rays varies substantially by X-ray energy. We show this explicitly in Fig. 2: a 100-eV photon has a MFP of 0.1–0.2 Mpc, whereas a 1-keV photon has a MFP that is larger by more than three orders of magnitude. Note too the ‘ranking’ of the three species in this plot – He I has the lowest MFP at all energies, representing the bottleneck for X-rays that results in secondary ionizations for H I (Section 2).

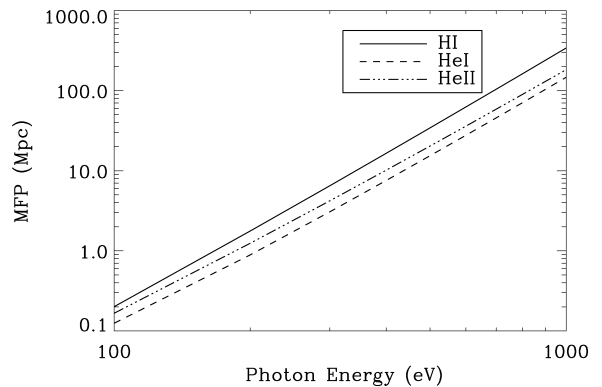


**Figure 2.** The MFP in Mpc for H I, He I and He II at  $z = 10$  for photon energies ranging from 0.1 to 1 keV.

### 3.1 Feedback from the first stars and QSOs

We begin by examining a number of cases at  $z = 10$  that involve varying combinations of starburst and BH masses. The plots all show cases with and without X-rays, and one with X-rays only (i.e. no lower energy photons). We begin with a  $10^5$ - $M_\odot$  starburst with a  $10^6$ - $M_\odot$  BH, hereinafter referred to as the standard case. Fig. 3 displays the ionization and temperature profiles as a function of distance from the central starburst/QSO source at  $z = 10$ , for the

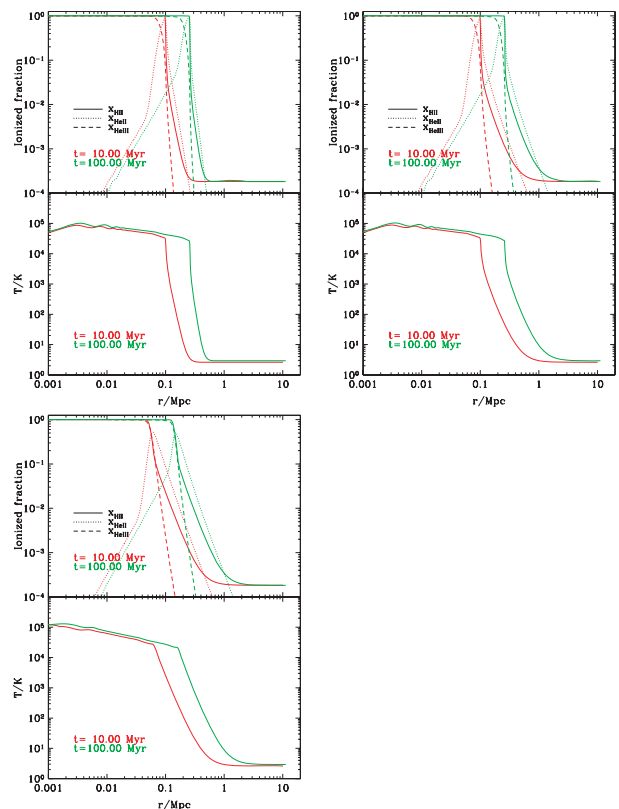


**Figure 3.** The ionization and temperature profiles for a  $10^5$ - $M_\odot$  starburst with a  $10^6$ - $M_\odot$  QSO/BH at  $z \sim 10$  (our standard case). The solid, dotted and dashed lines represent the fraction of H II, He II and He III, respectively. The red and green curves show the curves at times 10 and 100 Myr after the quasar turns on. The upper left-hand and upper right-hand panels display the cases with the full QSO spectrum with UV photons, but that exclude and include X-rays from the central QSO. The lower panel shows the effects arising from X-rays alone.

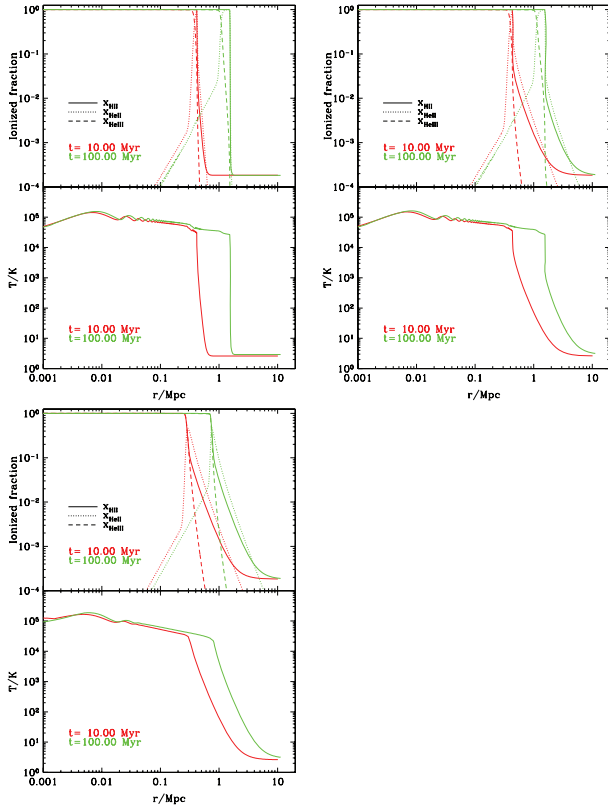


**Figure 4.** The ionization and temperature profiles for a  $10^5$ - $M_{\odot}$  starburst with a  $10^8$ - $M_{\odot}$  QSO/BH at  $z \sim 10$ .

species H II, He II and He III. The red and green curves, respectively, show the evolution of the ionization and temperature curves at times 10 and 100 Myr after the source turns on. The X-rays contribute from  $\sim$ a few per cent up to full ionization in different H/He species at IGM scales (10–100 kpc) and heating of the order of  $10^4$ – $10^5$  K. Although the panels with and without X-rays (the upper two panels) look very similar at first glance, we note the extended tail of low-level ionization in H II and He II (but not He III) beyond the I-front: the signature of X-ray ionization. This can be seen in the red curves (10 Myr) on physical scales of 0.1–0.2 Mpc.

We also consider cases where the BH mass and QSO duty cycle are varied. This reveals the various contributions more clearly, particularly that from X-rays. The results are shown in Figs 4–6, where we can see that increasing (or decreasing) the BH mass or the duty cycle simply ‘dials up’ (or ‘dials down’) the effects of ionization. For the higher BH mass, the X-ray I-fronts advance further and reach higher values of ionization. Nevertheless, the high temperatures of  $10^6$  K and strong ionization effects from X-rays at large scales found by some authors, for example, Thomas & Zaroubi (2008), are not reproduced here, possibly arising from differences in model assumptions and input spectra (discussed further in Section 3.3).

Comparing the curves for the X-ray-only case for the QSO/BH masses of 0,  $10^3$  and  $10^8$   $M_{\odot}$ , we see that X-rays *can* make a difference. Perhaps X-rays can become competitive with UV ionization only when the BH masses approach  $10^8$   $M_{\odot}$ . Note that such high QSO/BH masses are very rare at  $z = 10$  (Fig. 1), and likely non-existent at  $z = 20$  when the universe is younger and there has been little time to gain mass for a seed BH accreting at rates close to the Eddington value. Such  $10^8$ - $M_{\odot}$  or higher mass AGNs therefore

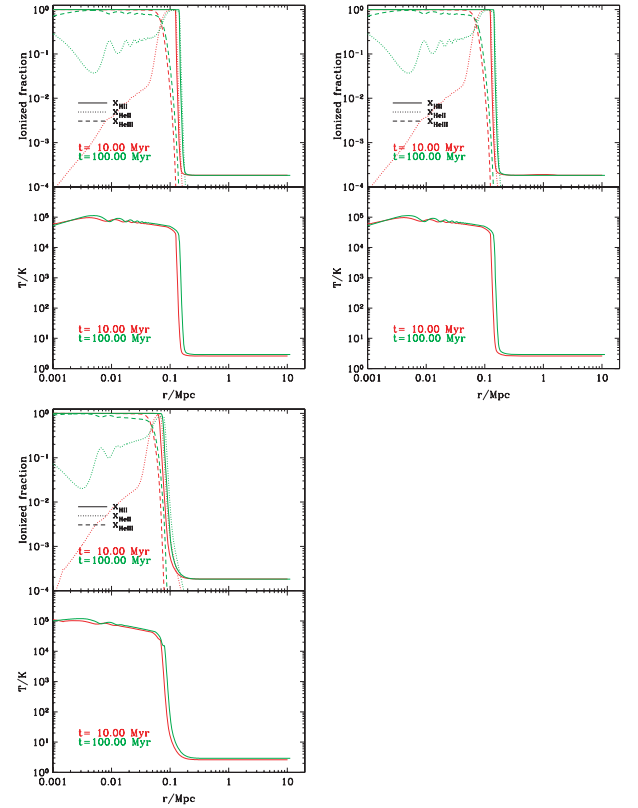


**Figure 5.** The ionization and temperature profiles for a  $10^6$ - $M_{\odot}$  starburst only (no QSO/BH) at  $z \sim 10$ .

may not contribute significantly to a cosmic X-ray background at  $z \gtrsim 10$ . Also, we point out that in all the figures, the X-ray-related features noted earlier (the tail of low-level ionization in H II and He II, but not He III, at large radii) are evident in the upper two panels in each case. The exception is the case with only stars ( $10^6$ - $M_{\odot}$  starburst, BH mass of 0  $M_{\odot}$ ) where the figures with and without X-rays are (unsurprisingly) near-identical.

Additionally, we ran cases with smaller masses in stars and BHs. One such case is shown in Fig. 6, where the ionization and temperature profiles are displayed for a  $10^3$ - $M_{\odot}$  starburst with a  $10^4$ - $M_{\odot}$  BH at  $z \sim 10$ , at times 10 and 100 Myr after the quasar turns on. Unlike previous figures in the paper, the no-X-ray case is not shown here, as it is very similar to the full-spectrum case. The various panels show the curves for the full QSO spectrum (including UV/X-ray photons) and with X-rays only, with varying QSO duty cycles of 10 and 100 Myr. The ionization and maximum temperatures are lower over 10–100 kpc compared with our standard case, but the role of X-rays for He I ionization is more clearly seen here than in most of our cases, particularly in the X-ray-only panel for a QSO duty cycle of 100 Myr.

Other trends include variations with time or between species. Allowing the QSO/starburst source to be ‘on’ for 100 Myr advances the I-fronts for all cases and species relative to the curves for 10 Myr, as expected. The temperatures, however, increase notably at 100 Myr only for the pure-X-ray case; for the cases involving the full spectrum or without X-rays, the temperatures appear to saturate at a few tens of thousands of K, and having the source on for longer time-scales makes little difference. In addition, the He III I-front mostly lags the H I front, but in some cases, the He III front almost catches

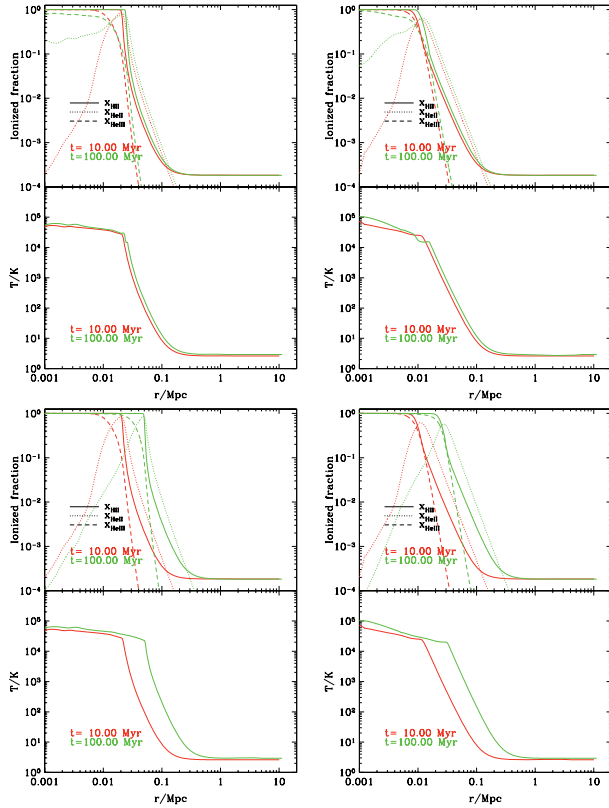


**Figure 6.** The ionization and temperature profiles for a  $10^3$ - $M_{\odot}$  starburst with a  $10^4$ - $M_{\odot}$  QSO/BH at  $z \sim 10$ . The left-hand and right-hand panels in each row display the cases with the full QSO spectrum (including UV/X-ray photons) and with X-rays only. The upper row has a QSO duty cycle of 10 Myr and the lower row has a QSO duty cycle of 100 Myr. The red and green curves show the curves at times 10 and 100 Myr after the quasar turns on. Unlike previous figures in this paper, the no-X-ray case is not shown here, as it is very similar to the full-spectrum case.

up with the H I front. Thus, it appears that these species' I-fronts can be coincident for sufficiently hard radiation.

The He II ionization fraction exceeds that of H I by a small margin, particularly beyond the edge of the UV I-front. We recognize this as the characteristic tail of added secondary ionizations from X-rays, which manifest more strongly at larger physical scales where the UV photons do not penetrate as far. This can be seen best by comparing the no-X-ray and X-ray-only panels of all the figures in this section, where the He II front lags or is similar to the H I front when X-rays are absent but leads the H I front when only X-rays are present. This interplay between the X-ray secondary ionization and the ionization balance of H and He in the presence of hard radiation leads to ionization boundaries that are less sharp than in the UV-ionization case alone (see also Furlanetto & Oh 2008b on this point in relation to the morphology of helium reionization at lower redshifts,  $z \sim 3$ ). Lastly, in the case with only a  $10^6$ - $M_{\odot}$  starburst (Fig. 5), we see that there is little difference between these two panels, as this case has low X-ray production.

To test the variation with redshift, we perform the same calculations for our standard case assumptions at  $z = 20$ . Exploring redshifts lower than  $z \sim 10$  marks the era of overlapping I-fronts as reionization draws to an end, which our current treatment cannot model well. Additionally, there is not much H I remaining outside galaxy haloes to generate an interesting 21-cm signal at the end of reionization, whereas the 21-cm signal is expected to be significant

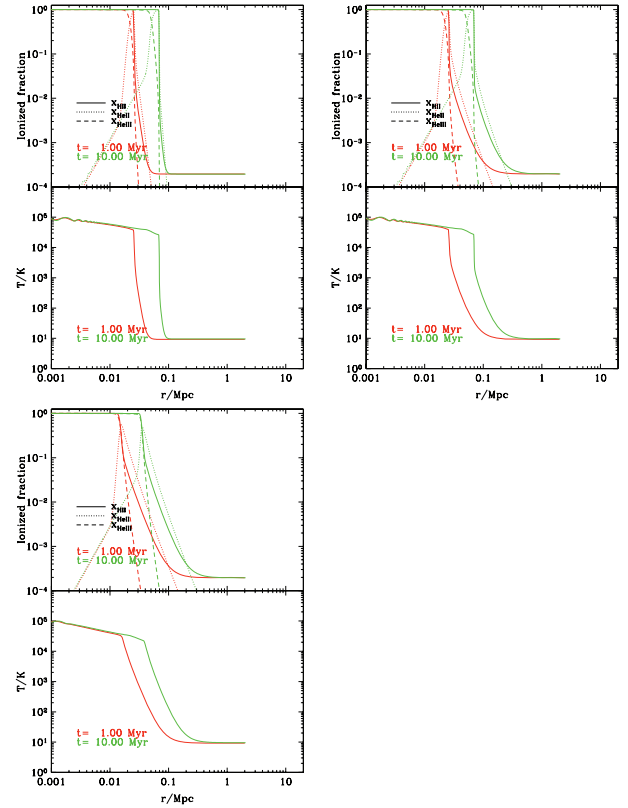


**Figure 7.** The ionization and temperature profiles for a  $10^5$ - $M_{\odot}$  starburst with a  $10^6$ - $M_{\odot}$  QSO/BH at  $z = 20$ . The legend is the same as in earlier figures. See text for explanation. The curves are shown for the time-scales of 1 and 10 Myr (rather than 10 and 100 Myr as in all preceding figures), owing to the shorter IGM recombination time-scales at  $z = 20$  relative to those at  $z = 10$ .

at  $z = 10$ – $20$ . The calculations at  $z = 20$  for our standard case are displayed in Fig. 7 with the same three panels as in the ionization and temperature figures. As the IGM is denser and the recombination time-scales are shorter, we show curves for times at 1 and 10 Myr (rather than 10 and 100 Myr) after the source turns on. We see that the ionization curves at 10 Myr between the  $z = 20$  case and our standard case at  $z = 10$  have very similar shapes, with the  $z = 20$  curves lagging the  $z = 10$  curves, expected from the higher IGM densities at earlier times. Note, however, that the peak temperatures achieved in all of these cases remain similar, around  $10^5$  K.

We perform a simple estimate of the trade-off between the local X-ray flux from a single galaxy versus the X-rays from a number of distant sources. The comoving number density of haloes in our work with masses  $\gtrsim 10^8 M_{\odot}$  is  $n = 1.147 (6.443 \times 10^{-4}) \text{ Mpc}^{-3}$  at  $z = 10$  (20). This translates to an average spacing between such haloes of  $\sim 0.95$  (11.5) Mpc at  $z = 10$  (20). The emission rate of H-ionizing photons for a  $10^5$ - $M_{\odot}$  starburst with a  $10^6$ - $M_{\odot}$  BH (our typical case)<sup>6</sup> is  $S \sim 1.3 \times 10^{51}$  photons  $\text{s}^{-1}$ . The associated X-ray photon production rate is  $\sim 1.3 \times 10^{49}$  ( $2.1 \times 10^{48}$ ) photons  $\text{s}^{-1}$  at 300 eV (1 keV). If we assume a uniform IGM with no attenuation and that the visibility sphere for sources can go out to a maximum

<sup>6</sup> For comparison,  $S \sim 0.43 \times 10^{51}$  photons  $\text{s}^{-1}$  for a single  $200$ - $M_{\odot}$  star in Chen & Miralda-Escudé (2008),  $S \sim 10^{52}$  photons  $\text{s}^{-1}$  in Ricotti et al. (2005) (from the discussion related to their equation 4) and  $S \sim 10^{50}$ – $10^{54}$  photons  $\text{s}^{-1}$  for the BH mass range of  $10^3$ – $10^6 M_{\odot}$  considered in Thomas & Zaroubi (2008).

radius given by the MFP derived for X-rays as a function of energy in Fig. 2, then the critical distance from an individual galaxy source at which the flux of the source becomes equal to the background flux from sources of similar individual fluxes is 0.1–0.5 Mpc at  $z = 10$  for 300 eV to 1 keV X-rays. Thus, our results at  $z = 10$ , for example, in Fig. 3, could have additional contributions to X-ray ionization from neighbouring galaxy haloes at radii 0.1–1 Mpc, although this will be less of an issue at  $z = 20$ . In reality, we need to factor in realistic density profiles for the galaxies and the IGM, as well as the time-variability of individual sources. We will pursue this in future work involving a full cosmological calculation through extensions to the current GALACTICUS code (see Section 4).

Finally, we note the oscillations in the He II fraction and temperature profiles in some of our models. We performed a number of checks to make sure these were not mere numerical effects. We found that these oscillations are robust to increases in time resolution, ordinary differential equation solver accuracy and the number of radial shells used in our code. These oscillations are also well resolved radially and have a near-constant wavelength, despite the logarithmically spaced grid spacing in radius. What may be occurring is similar to the physics of the instability strip in stellar atmospheres. Inside the ionized region, the optical depth is very small, so the incident flux drops as  $1/r^2$ . The small H I, He I and He II fractions are determined by the balance between photoionization, collisional ionization and recombination rates, while the temperature is controlled by the balance between photoheating and cooling rates. As we move outwards in radius, this leads to a complex interplay between the photoheating rate, temperature and the He II fraction in the region of the He III to He II transition, leading to the temperature and He II fraction oscillating with radius. This arises from our solving the time-dependent ionization and heating equations rather than adopting the equilibrium solution. Given several of our idealized approximations here, such as spherical symmetry, we do not expect this effect to have a significant impact, particularly on the 21-cm signal which we discuss next.

### 3.2 Radio signatures

Over the last decade, there has been a growing literature on the 21-cm radio signals arising from the percolation of reionization, that is, the growth of ionized bubbles around the first luminous sources and the associated heating (Chen & Miralda-Escudé 2004, 2008; Furlanetto et al. 2004, 2004; Zaldarriaga, Furlanetto & Hernquist 2004; Furlanetto & Pritchard 2006; Furlanetto, Oh & Briggs 2006; Kuhlen, Madau & Montgomery 2006; McQuinn et al. 2006; Pritchard & Furlanetto 2007; Ripamonti et al. 2008; Santos et al. 2008; Thomas & Zaroubi 2008; Morales & Wyithe 2010). The signature is expected to be absorption (emission) against the CMB if the ionized region is colder (warmer) than the CMB at those epochs. Forthcoming interferometric experiments at radio wavelengths, such as the LOFAR and SKA, are predicted to be able to resolve ionized bubbles of size  $\sim 100$  kpc up to a few Mpc. The dominant signal arises from the coupling of the spin temperature of neutral hydrogen with the kinetic temperature of the background IGM gas. After recombination, the IGM cools as  $(1+z)^2$ , whereas the CMB cools as  $(1+z)$ , leading to a 21-cm absorption signal from the neutral IGM gas. At later epochs, the spin states of hydrogen come into equilibrium with the CMB, leading to a decreasing 21-cm signal. As the first stars and quasars turn on, a 21-cm emission signal is generated through coupling the spin states with the scattering of Ly $\alpha$  photons and other processes.

Here, we follow the formalism outlined in Chen & Miralda-Escudé (2008). As we do not follow the detailed cosmological evolution of a distribution of ionized bubbles, we model the spin temperature of H I at a fixed redshift as

$$T_s = \frac{T_{\text{CMB}} + (y_\alpha + y_c)T_k}{1 + y_\alpha + y_c}, \quad (17)$$

where  $T_{\text{CMB}}$  is the CMB temperature at that redshift ( $z = 10$  in our cases, unless otherwise specified) and  $T_k$  is the gas kinetic temperature (which is a function of distance from the source). The  $y$  coefficients are related to the coupling arising from Ly $\alpha$  photons ( $y_\alpha$ ) and from collisions ( $y_c$ ). The coefficient  $y_c$  is taken from Chen & Miralda-Escudé (2008) and Kuhlen et al. (2006). The coefficient  $y_\alpha$  is the Ly $\alpha$  coupling term arising from the Wouthysen–Field effect. We use the expressions for  $y_\alpha$  from Chen & Miralda-Escudé (2008), Zaldarriaga et al. (2004) and Pritchard & Furlanetto (2007), with additional parameters from Hirata (2006). In the cases considered here, Ly $\alpha$  coupling dominates over other terms such as collisional coupling. We specifically include the Ly $\alpha$  photons from the stars and/or QSO emission in our models, as well as the auxiliary Ly $\alpha$  photons arising from X-ray ionization (Shull & van Steenberg 1985; Venkatesan et al. 2001; Chen & Miralda-Escudé 2008).

This leads to a brightness temperature (measured as a differential from the background CMB temperature at that epoch) given by

$$\delta T_b = 40 \text{ mK} \frac{\Omega_b h_0}{0.03} \sqrt{\frac{0.3}{\Omega_0}} \sqrt{\frac{1+z}{25}} \frac{\rho_{\text{H I}}}{\bar{\rho}_{\text{H}}} \frac{T_s - T_{\text{CMB}}}{T_s}. \quad (18)$$

When this calculated brightness temperature,  $\delta T_b$ , lies above the CMB temperature at that epoch, the ionized region will be seen in emission against the CMB. Conversely, regions beyond the I-front that lie below the CMB temperature will be seen in absorption against the CMB.

In Figs 8–13, we show the temperature profiles with radius for the spin temperature and gas kinetic temperature relative to the

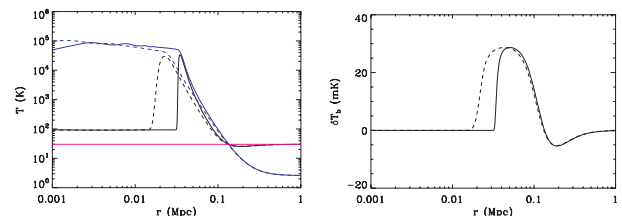


**Figure 8.** Left-hand panel: the temperature profiles with radius for the spin temperature (black curves), kinetic temperature (blue curves) and the CMB temperature (purple line). Right-hand panel: the 21-cm brightness temperature profile. All cases are for a  $10^5$ - $M_\odot$  starburst with a  $10^6$ - $M_\odot$  QSO/BH at  $z = 10$ , at times of 1 Myr after the burst/QSO turns on. In each case, the solid lines are for the full-spectrum case (X-rays and UV radiation) and the dashed lines are for X-rays only.

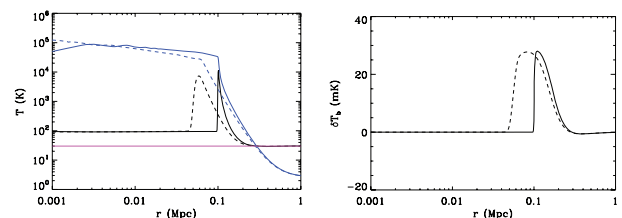


**Figure 9.** The temperature profiles (left-hand panel) and 21-cm brightness temperature profile (right-hand panel) are shown for a  $10^5$ - $M_\odot$  starburst with a  $10^6$ - $M_\odot$  QSO/BH at  $z = 10$ , at times of 10 Myr (rather than 1 Myr) after the burst/QSO turns on. The legend is the same as for Fig. 8.

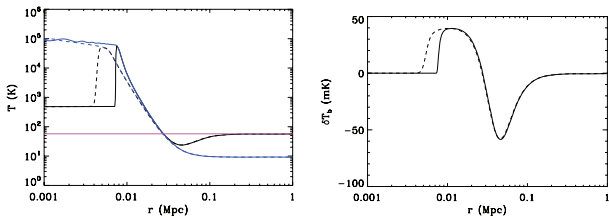


**Figure 10.** The temperature profiles (left-hand panel) and 21-cm brightness temperature profile (right-hand panel) are shown for a  $10^5\text{-}M_\odot$  starburst with a  $10^6\text{-}M_\odot$  QSO/BH at  $z = 20$ , at times of 0.1 Myr after the burst/QSO turns on. The legend is the same as for Fig. 8. Note the deeper trough in  $\delta T_b$  (relative to the same case at  $z = 10$ ) in the absorption signal against the CMB at scales of approximately a few tens of kpc.

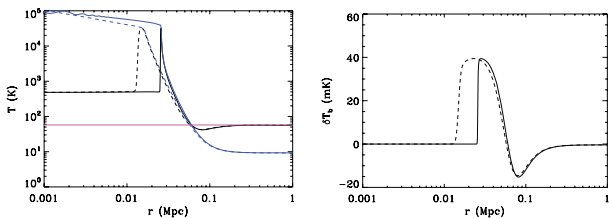


**Figure 11.** The temperature profiles (left-hand panel) and 21-cm brightness temperature profile (right-hand panel) are shown for a  $10^5\text{-}M_\odot$  starburst with a  $10^6\text{-}M_\odot$  QSO/BH at  $z = 20$ , at times of 1 Myr (rather than 0.1 Myr) after the burst/QSO turns on. The legend is the same as for Fig. 8.

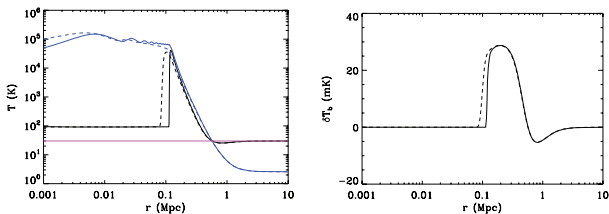


**Figure 12.** The temperature profiles (left-hand panel) and 21-cm brightness temperature profile (right-hand panel) are shown for a  $10^5\text{-}M_\odot$  starburst with a  $10^8\text{-}M_\odot$  QSO/BH at  $z = 10$ , at times of 1 Myr after the burst/QSO turns on. The legend is the same as for Fig. 8.

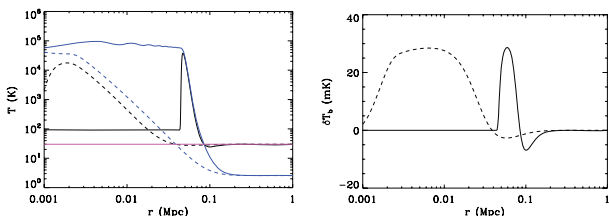


**Figure 13.** The temperature profiles (left-hand panel) and 21-cm brightness temperature profile (right-hand panel) are shown for a  $10^6\text{-}M_\odot$  starburst with no QSO/BH at  $z = 10$ , at times of 1 Myr after the burst turns on. The legend is the same as for Fig. 8. The difference is more pronounced between the cases with only X-rays versus X-rays and UV radiation, owing to the low X-ray production of stars in our models.

CMB temperature which is constant at a fixed redshift. We also show the 21-cm brightness temperature profile and include the full-spectrum case (X-ray and UV photons) and X-ray-only cases for each set of curves. These scenarios span most of the cases discussed in Section 3.1, involving a combination of starburst and QSO/BH masses (most of which are at  $z = 10$ , with two cases at  $z = 20$ ).

Some broad conclusions that are common to all the cases whose 21-cm signatures are shown are as follows. First, the curves for the spin temperature are characteristically peaked around the location of the stalled I-front. The transition from fully ionized within (with zero  $\delta T_b$ ) to the neutral IGM gas occurs beyond the I-front in each case, with peak values for  $T_s$  reaching  $\sim 10^4\text{--}10^5$  K in our cases, and peak values for the  $\delta T_b$  emission signal reaching around 30–40 mK. Negative  $\delta T_b$  values, corresponding to an absorption signal relative to the CMB, occur on scales between 0.1 and 1 Mpc at  $z = 10$  in our models and have low net values of  $\sim 0$  to a few mK, and larger values of  $\sim 20\text{--}60$  mK on scales of 0.01–0.1 Mpc at  $z = 20$ . We discuss this further below.

Secondly, the curves in each case corresponding to the X-ray-only case for each starburst/BH scenario consistently *lag* the curves for the corresponding full-spectrum case. This is most dramatically seen in the star-only case (Fig. 13, a  $10^6\text{-}M_\odot$  starburst with no QSO/BH), where the X-ray production is low. Here, the maximum values of  $\delta T_b$  occur between 1 and 10 kpc for the X-ray-only case and at about 50 kpc for the full-spectrum case. This case also reveals the inherently ‘fuzzy’ I-fronts associated with X-rays, relative to the sharp I-fronts of UV radiation – note the gradual transition in spin temperature for the X-ray-only case spanning nearly two orders of magnitude in scale. In contrast, the case of the  $10^5\text{-}M_\odot$  starburst with a  $10^8\text{-}M_\odot$  QSO/BH (Fig. 12) reveals that the cases with and without X-rays barely differ in the location and peak values of  $T_s$  and  $\delta T_b$  (emission in the latter). This arises directly in the strong contribution of X-rays to the overall ionization budget in this scenario. Ironically, it seems that the greater the X-ray production of a source, the less likely it is to have a *distinguishing* X-ray-related signature at 21 cm.

These results reveal one of the key goals of this paper: the difference in the topology of reionization between X-ray and UV ionization scenarios, and their impact on 21-cm predictions. Although X-rays do penetrate deeper into the IGM than do UV photons (leading to the moderate gains in ionization and temperature mentioned earlier), their ‘I-fronts’ trail the UV I-fronts and therefore the UV-associated 21-cm signal. This could therefore ‘blur’ the signatures of the growth of ionized bubbles around first-light sources and alter predictions for observing the percolation of reionization (see the semi-numerical simulations of Warszawański, Geil & Wyithe 2009 on this point). We note that a cosmological scenario in which X-rays alone are generated is not well motivated physically. Rather, the figures in this section show that the differing scale-dependent ionization from X-ray and UV photons leads directly to 21-cm signals that can be distinguished from each other.

We consider time-evolution in two cases for the same source of a  $10^5\text{-}M_\odot$  starburst with a  $10^6\text{-}M_\odot$  QSO/BH: at  $z = 10$  for the times of 1 and 10 Myr after the burst/QSO turns on (Figs 8 and 9), and at  $z = 20$  for the times of 0.1 and 1 Myr (Figs 10 and 11). The main effects of the advancing I-front with time on the 21-cm signal at a *fixed redshift* are the following: a similar advancing of the spin temperature curve’s peak and therefore that of  $\delta T_b$ , from a few tens of kpc to about 100 kpc, and a *decreased* peak value in  $T_s$ . This is mostly due to the rapid fall-off in the Ly $\alpha$  flux at increasing radii (going as  $r^{-2}$ ), which leads to a decreased coupling between the gas H I and the source radiation. The important role of this Ly $\alpha$  photon coupling is manifested also through the slight increase in the positive values (emission signal) of  $\delta T_b$  and the increased *negative* values of  $\delta T_b$  (absorption signal at 21 cm) at  $z = 20$  relative to  $z = 10$ , arising from the closer location of the I-fronts to the source with increasing redshift. These effects are discussed in more detail in the next section.

### 3.3 Comparison with other works

Here, we compare our results and model assumptions with those from papers in the recent literature addressing X-ray and/or helium ionization, and the resulting 21-cm signals. We find that our results are, for the most part, in agreement with the findings of other groups when we make similar model assumptions. We also comment on the theoretical assumption of passive X-ray production tied to star formation at high redshifts.

In Chen & Miralda-Escudé (2004) and Chen & Miralda-Escudé (2008), the emergent spectrum is based on a radiative transfer calculation starting with a stellar blackbody spectrum. There is no stated definition to distinguish between X-rays and UV radiation, so that (as in some works on this topic) it is unclear where the X-ray–UV photon boundary lies. To compare their results with ours, we started with the blackbody spectrum from equation (8) in Chen & Miralda-Escudé (2008). The range of Population III star masses that they consider (25–800  $M_{\odot}$ ) leads to a relatively narrow range of blackbody temperatures,  $T_{\text{eff}} \sim 1.06 \times 10^5$ – $1.17 \times 10^5$  K. In Fig. 14, we show the blackbody energy output (the Planck energy density, in units of power per unit area per unit solid angle per unit frequency) as a function of energy for a 25- and a 1000- $M_{\odot}$  star. There is little difference between the two cases – essentially nearly all Population III stars have the same energy output (Bromm, Kudritzki & Loeb 2001; Tumlinson et al. 2003).

However, what is relevant here for us is the cut-off between UV and X-ray photons. The strict definition of X-rays has a lower limit of 120 eV for X-ray energies. In Fig. 14, we see that the energy curves are relatively flat for energies of 20–40 eV and start to decline steeply above 100 eV. We were able to reproduce fig. 1 in Chen & Miralda-Escudé (2008) only for the X-ray threshold energy lying at about 30 eV. Such ‘X-rays’ can make a substantial addition to the UV-only ionization case, owing to the large numbers of photons below 100 eV. However, placing the cut-off at 100 eV or higher (where the spectrum is down by a factor of  $\sim 100$  relative to the peak) leads to the results in our earlier ionization figures, where X-rays can have a significant (but not dramatic) impact on IGM ionization and temperature.

Also, Chen & Miralda-Escudé (2008) consider a single 200- $M_{\odot}$  star embedded in a galaxy versus our treatment of a starburst and/or QSO as a point source in the IGM. The I-fronts in their work are therefore a factor of 10–20 closer to the source than in our results, leading directly to a lower Ly $\alpha$  flux in comparison at large scales

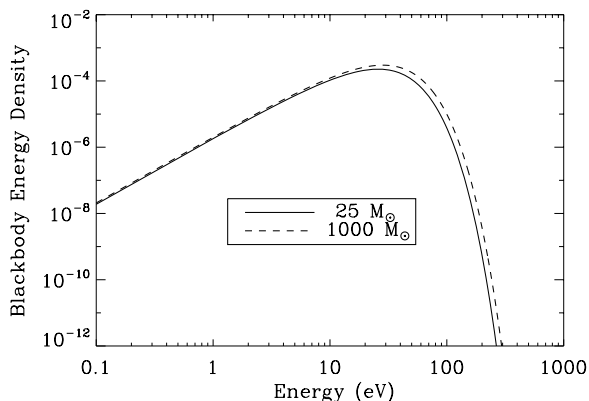


**Figure 14.** A comparison of the blackbody energy output (the Planck energy density, in units of power per unit area per unit solid angle per unit frequency) from a 25- and a 1000- $M_{\odot}$  star. Note the relative flatness of the curves at energies of 20–40 eV; beyond 100 eV, the curves decline steeply.

in our work. Consequently, the 21-cm *absorption* signal induced by the Ly $\alpha$  photons in our calculations is weaker relative to that in Chen & Miralda-Escudé (2008)<sup>7</sup> or, for example, Thomas & Zaroubi (2008). This reduced signal is seen as a minor dip, rather than a larger trough, in the 21-cm brightness temperature beyond the I-front location in the right-hand panels of the figures for the  $z = 10$  cases in Section 3.2. We have checked this by artificially placing the I-fronts in our cases in the 21-cm calculations at closer radii (by approximately a factor of 10) and are able to reproduce the 21-cm brightness temperature absorption signal of Chen & Miralda-Escudé (2008) and other works. Note that for the  $z = 20$ ,  $t = 0.1$  Myr case (Fig. 10), the absorption trough becomes more notable as the I-front has not advanced so far. This verifies the critical role of the inverse-square drop-off of the Ly $\alpha$  photon flux with distance from the source for 21-cm absorption (discussed in an earlier section). Note also that our results for the predicted amplitudes of the spin temperatures and the 21-cm *emission* signal are in agreement with other papers in the literature.

In Bolton et al. (2009), McQuinn et al. (2009), Furlanetto & Oh (2008b) and Furlanetto & Oh (2008a), the authors focus on He reionization by quasars at  $z \sim 3$ . Furlanetto & Oh (2008a) do not include the effects of X-ray heating in their calculations of helium ionization. Bolton et al. (2009) find a relatively modest gain in IGM temperature (of the order of  $10^4$  K) resulting from hard radiation, partly owing to the heating in underdense parts of the IGM (particularly fossil He III regions), achieving their maximal heating early on in the process of reionization (see also Venkatesan et al. 2003 on this point). This maximum IGM temperature of  $\sim 10^4$  K (comparable to the results of McQuinn et al. 2009) lies within the range of our findings, with the caveat that at  $z \sim 3$  the IGM is far less dense than at  $z \sim 10$ –20, and, additionally, the IGM hydrogen is completely reionized at  $z \sim 3$ , freeing up some of the UV photons and secondary electrons from He I ionization. We also compared our results with Kuhlen et al. (2006) – these authors do not include Ly $\alpha$  coupling in their 21-cm calculations, but we approximately reproduce their results on spin temperature values.

Thomas & Zaroubi (2008) have examined the feedback from early stellar populations and quasars, and the associated 21-cm signature. We found that we were unable to reproduce many of their results, including the high level of X-ray heating ( $T > 10^5$ – $10^6$  K) as well as the results in their figs 12 and 13. Some of this may arise from incomplete models of the high- $z$  galaxy distribution and that the stellar spectra have been simplified as a blackbody source. We do, however, find somewhat similar IGM temperatures and 21-cm brightness temperature values close to those computed in Ripamonti et al. (2008), although these authors focus on X-rays from BHs in the pre-reionization IGM. A direct comparison is challenging as we do not have a full cosmological calculation in this paper with a halo distribution function characterizing the ionization feedback.

Finally, Ricotti et al. (2005) consider the formation of a strong X-ray background generated at  $z \gtrsim 10$  by early BHs, with the specific aim of explaining the *WMAP* results of a (at the time high) electron scattering optical depth. In their work, the X-rays are created by accretion on to ‘seed’ BHs that are assumed to have formed from earlier generations of Population III stars. Hence, the total X-ray emissivity is proportional to the total mass in such BHs in high- $z$  haloes, which is in turn proportional to the total mass in

<sup>7</sup> See these authors’ discussion in Section 2 of their paper of the typical size of Ly $\alpha$  spheres in their work, being a few tens of kpc, and of their assumption that the fraction of X-ray energy converted to Ly $\alpha$  photons is 100 per cent.

Population III stars, that is, the production rate of X-rays is tied effectively to the star formation efficiency in high- $z$  galaxies (through the BH accretion rate). This is an assumption made in a number of papers, for example, Santos et al. (2008) who examined the role of inhomogeneous X-ray and Ly $\alpha$  radiation fields at  $z > 10$  for 21-cm signatures of H reionization. However, it remains to be seen how well this series of connections hold at the low BH masses anticipated in the first galaxies (e.g. do these low-mass BHs even accrete at the Eddington rate?). The Magorrian relation may not hold at low to moderate BH masses in galaxies (Greene et al. 2010), making the scaling of X-ray production with star formation rates and BH masses more ambiguous at low BH masses.

Ricotti et al. (2005), like Chen & Miralda-Escudé (2008), do not explicitly distinguish between soft X-ray and hard UV photons in their calculations. In these works, the boundary between UV and X-ray photons is related to the local column density of absorbers and the emergent power spectrum after radiative transfer, with the column density being a free parameter. Another important related parameter is the escape fraction of ionizing radiation,  $f_{\text{esc}}$ , for X-ray and UV photons, which is effectively calculated locally through the emerging flux at each radius (or cell) in our work and for the above papers. Variations in parameters such as the local absorber column density,  $f_{\text{esc}}$ , and reduced gas densities within galaxies owing to feedback effects could harden the source spectrum within the ionization bubbles, leading to potentially higher temperatures than we have found here. Although there is no straightforward way within the scope of our semi-analytic work to directly reproduce local  $f_{\text{esc}}$  and density-feedback effects from numerical simulations, we mention these caveats and note that we *are* able to reproduce the results of Chen & Miralda-Escudé (2008) by lowering the X-ray–UV boundary to 30 eV or placing the I-fronts closer to the source, both of which effectively harden the local ionizing spectra. Finally, Ricotti et al. (2005), Chen & Miralda-Escudé (2008) and Thomas & Zaroubi (2008) have a fully cosmological calculation that keeps track of the evolving spectra of stellar and QSO populations. Therefore, soft X-rays from high- $z$  sources are redshifted and can become important for hard UV ionization at later epochs. Our current results do not factor in this effect, but we plan to extend this work in the near future to fully cosmological calculations that include realistic galaxy profiles and the redshift evolution of galaxy haloes and their radiation fields.

#### 4 CONCLUSIONS

We have examined the effects of X-rays from high-redshift quasars and stars when acting in combination with hard UV ionizing radiation from these sources. We find that, relative to hard UV radiation, X-rays may not dominate the ionization and thermal history of the IGM, and contribute modest increases to the IGM ionization at  $z \sim 10$  and of the order of  $10^3$ – $10^5$  K to the IGM temperatures. This is in contrast with some earlier works in which X-rays could cause IGM heating up to  $10^6$  K and near-total reionization at  $z = 10$ – $20$ . While some of this may be due to our simplified models, we believe that most of the difference between our results (where we include the X-rays coming from individual sources), and those of other works deriving high IGM temperatures and ionization from X-rays at  $z = 10$ – $20$ , arises from the latter’s assumption of strong X-ray production that is tied to the star formation rate at high redshift.

We also examined the 21-cm signatures of various cases involving combinations of stars and BH masses, and find that the 21-cm signal of X-ray versus UV ionization could be distinct, resulting from their differing contributions to the topology of reionization.

We find that the brightness temperature emission expected from X-rays alone occurs at smaller scales than that from UV radiation. The different spatial scales at which they manifest may therefore ‘blur’ the 21-cm signature of the percolation of reionization around early haloes, depending on whether a cosmic X-ray or UV background is built up first. An X-ray background may not significantly precede a UV background, as a typical X-ray photoionization time-scale exceeds the Hubble time for  $z \gtrsim 10$ . From our simplified treatment, it is unclear whether there is a cosmological epoch when the IGM’s thermodynamic and ionization properties are determined mostly by X-rays. The role of X-rays versus hard UV radiation can also be tested through their interactions with the CMB, where the relative strengths of their contributions to reionization as well as the redshifts that they dominantly contribute at can be constrained through the CMB polarization power spectrum at large angular scales. The currently operating all-sky CMB mission *Planck* may be able to distinguish such scenarios.

For sufficiently hard radiation from sources, the H II and He III I-fronts may lie very close to each other. Although our calculation is 1D in nature, this result will impact the escape fraction of ionizing radiation from primordial galaxies, and the geometry of bubbles and chimneys as ionization proceeds from these galaxies. We hope to examine this problem in a future work.

To further explore the evolution of first-light sources and the IGM with redshift, we will extend our current calculations using the *GALACTICUS* code to a fully cosmological framework that includes evolving dark matter haloes, galaxy/BH formation and evolving stellar/QSO populations with time-dependent radiation fields. This will permit a self-consistent calculation of IGM reionization and allow us to derive predictions for the growth and evolution of a cosmologically representative distribution of ionized bubbles as a function of redshift. We can also calculate the bubbles’ thermal properties, as well as the statistical properties of the bubble population, such as the mean size of ionized and neutral regions and power spectra of 21-cm emission or absorption relative to the CMB (utilizing the known correlation properties of the dark matter haloes which host the sources). Such predictions will be tested by data from CMB space telescopes, such as *Planck*, and ground-based radio telescopes that are designed to map the percolation of reionization around first-light sources. These observations, coupled with our detailed theoretical predictions, will additionally place strong constraints on the populations of ionizing sources at intermediate to high redshifts and therefore on the properties of early generations of galaxies and AGNs. The resulting improvements in our understanding of these early objects will permit more robust predictions to be made for other observing programmes, such as those of *The James Webb Space Telescope*, which will probe similar galaxy/QSO populations.

#### ACKNOWLEDGMENTS

AV gratefully acknowledges support from the Research Corporation through the Single Investigator Cottrell College Science Award and from the University of San Francisco Faculty Development Fund. AB acknowledges the support of the Gordon & Betty Moore Foundation. We thank the referee for a constructive report, and Massimo Ricotti, Xuelei Chen and Steve Furlanetto for useful input.

#### REFERENCES

- Aldrovandi S. M. V., Pequignot D., 1973, *A&A*, 25, 137  
 Arnaud M., Rothenflug R., 1985, *A&AS*, 60, 425

- Barkana R., Loeb A., 1999, *ApJ*, 523, 54
- Benson A. J., 2011, *New Astron.*, in press
- Benson A. J., Bower R., 2010, *MNRAS*, 405, 1573
- Benson A. J., Frenk C. S., Lacey C. G., Baugh C. M., Cole S., 2002a, *MNRAS*, 333, 177
- Benson A. J., Lacey C. G., Baugh C. M., Cole S., Frenk C. S., 2002b, *MNRAS*, 333, 156
- Benson A. J., Sugiyama N., Nusser A., Lacey C. G., 2006, *MNRAS*, 369, 1055
- Bolton J. S., Oh S. P., Furlanetto S. R., 2009, *MNRAS*, 395, 736
- Bromm V., Kudritzki R. P., Loeb A., 2001, *ApJ*, 552, 464
- Bullock J. S., Kravtsov A. V., Weinberg D. H., 2000, *ApJ*, 539, 517
- Busha M. T., Alvarez M. A., Wechsler R. H., Abel T., Strigari L. E., 2010, *ApJ*, 710, 408
- Chen X., Miralda Escudé J., 2004, *ApJ*, 602, 1
- Chen X., Miralda Escudé J., 2008, *ApJ*, 684, 18
- Chiu W. A., Ostriker J. P., 2000, *ApJ*, 534, 507
- Ciardi B., Ferrara A., Governato F., Jenkins A., 2000, *MNRAS*, 314, 611
- Dawson S., Rhoads J. E., Malhotra S., Stern D., Wang J., Dey A., Spinrad H., Jannuzi B. T., 2007, *ApJ*, 671, 1227
- Dayal P., Maselli A., Ferrara A., 2011, *MNRAS*, 410, 830
- Efstathiou G., 1992, *MNRAS*, 256, 43P
- Furlanetto S. R., Oh S. P., 2008a, *ApJ*, 682, 14
- Furlanetto S. R., Oh S. P., 2008b, *ApJ*, 681, 1
- Furlanetto S. R., Pritchard J. R., 2006, *MNRAS*, 372, 1093
- Furlanetto S. R., Zaldarriaga M., Hernquist L., 2004, *ApJ*, 613, 16
- Furlanetto S. R., Oh S. P., Briggs F. H., 2006, *Phys. Rep.*, 433, 181
- Gardner J. P. et al., 2009, in Thronson H. A., Stiavelli M., Tielens A. G. G. M., eds, *Astrophysics in the Next Decade*. Springer, Utrecht
- Gnedin N. Y., Ostriker J. P., 1997, *ApJ*, 486, 581
- Greene J. E. et al., 2010, *ApJ*, 721, 26
- Gültekin K. et al., 2009, *ApJ*, 698, 198
- Haardt F., Madan P., 1996, *ApJ*, 461, 20
- Hirata C. M., 2006, *MNRAS*, 367, 259
- Hopkins P. H., 2011, *MNRAS*, submitted
- Kereš D., Katz N., Weinberg D. H., Davé R., 2005, *MNRAS*, 363, 2
- Koposov S. E., Yoo J., Rix H., Weinberg D. H., Macci A. V., Miralda Escudé J., 2009, *ApJ*, 696, 2179
- Kuhlen M., Madau P., Montgomery R., 2006, *ApJ*, 637, L1
- Larson D. et al., 2011, *ApJS*, 192, 16
- Loeb A., 2009, in Thronson H. A., Stiavelli M., Tielens A. G. G. M., eds, *Astrophysics in the Next Decade*. Springer, Utrecht
- Loeb A., Barkana R., 2001, *ARA&A*, 39, 19
- Macci A. V., Kang X., Fontanot F., Somerville R. S., Koposov S., Monaco P., 2010, *MNRAS*, 402, 1995
- McQuinn M., Zahn O., Zaldarriaga M., Hernquist L., Furlanetto S. R., 2006, *ApJ*, 653, 815
- McQuinn M., Lidz A., Zaldarriaga M., Hernquist L., Hopkins P. F., Dutta S., Faucher-Giguère C.-A., 2009, *ApJ*, 694, 842
- Madau P., 1995, *ApJ*, 441, 18
- Meiksin A., 2006, *MNRAS*, 365, 807812
- Morales M. F., Wyithe J. S. B., 2010, *ARA&A*, 48, 127
- Muoz J. A., Madau P., Loeb A., Diemand J., 2009, *MNRAS*, 400, 1593
- Navarro J. F., Steinmetz M., 1997, *ApJ*, 478, 13
- Oh S. P., Haiman Z., Rees M. J., 2001, *ApJ*, 553, 73
- Onken C. A., Miralda Escudé J., 2004, *ApJ*, 610, 1
- Peebles P. J. E., 1968, *ApJ*, 153, 1
- Pritchard J. R., Furlanetto S. R., 2007, *MNRAS*, 376, 1680
- Quinn T., Katz N., Efstathiou G., 1996, *MNRAS*, 278, L49
- Ricotti M., Ostriker J. P., Gnedin N. Y., 2005, *MNRAS*, 357, 207
- Ricotti M., Ostriker J. P., Mack K. J., 2008, *ApJ*, 680, 829
- Ripamonti E., Mapelli M., Zaroubi S., 2008, *MNRAS*, 387, 158
- Santos M. G., Amblard A., Pritchard J., Trac H., Cen R., Cooray A., 2008, *ApJ*, 689, 1
- Scholz T. T., Walters H. R. J., 1991, *ApJ*, 380, 302
- Seager S., Sasselov D. D., Scott D., 2000, *ApJS*, 128, 407
- Shull J. M., van Steenberg M., 1982, *ApJS*, 48, 95
- Shull J. M., van Steenberg M. E., 1985, *ApJ*, 298, 268
- Sokasian A., Abel T., Hernquist L., Springel V., 2003, *MNRAS*, 344, 607
- Somerville R. S., 2002, *ApJ*, 572, L23
- Somerville R. S., Bullock J. S., Livio M., 2003, *ApJ*, 593, 616
- Spitzer L., 1978, *Physical Processes in the Interstellar Medium*. Wiley, New York
- Springel V. et al., 2005, *Nat*, 435, 629
- Sutherland R. S., 1998, *MNRAS*, 300, 321
- Thomas R. M., Zaroubi S., 2008, *MNRAS*, 384, 1080
- Tumlinson J., Giroux M. L., Shull J. M., 2001, *ApJ*, 550, L1
- Tumlinson J., Shull J. M., Venkatesan A., 2003, *ApJ*, 584, 608
- Tumlinson J., Venkatesan A., Shull J. M., 2004, *ApJ*, 612, 602
- Venkatesan A., Giroux M. L., Shull J. M., 2001, *ApJ*, 563, 1
- Venkatesan A., Tumlinson J., Shull J. M., 2003, *ApJ*, 584, 621
- Verner D. A., Ferland G. J., 1996, *ApJS*, 103, 467
- Verner D. A., Yakovlev D. G., 1995, *A&AS*, 109, 125
- Verner D. A., Ferland G. J., Korista K. T., Yakovlev D. G., 1996, *ApJ*, 465, 487
- Voronov G. S., 1997, *At. Data Nucl. Data Tables*, 65, 1
- Warszawski L., Geil P. M., Wyithe J. S. B., 2009, *MNRAS*, 396, 1106
- Wise J. H., Turk M. J., Abel T., 2008, *ApJ*, 682, 745
- Wyithe J. S. B., Loeb A., 2003, *ApJ*, 586, 693
- Zaldarriaga M., Furlanetto S. R., Hernquist L., 2004, *ApJ*, 608, 622

This paper has been typeset from a  $\text{\TeX}/\text{\LaTeX}$  file prepared by the author.